Journal of Materials Chemistry A



PAPER

View Article Online
View Journal | View Issue



Cite this: J. Mater. Chem. A, 2022, 10, 18657

Received 1st June 2022 Accepted 15th July 2022

DOI: 10.1039/d2ta04365c

rsc.li/materials-a

A waterbomb origami tower for convertible photothermal evaporation[†]

Xiaojie Liu, Yanpei Tian, Fangqi Chen, Ying Mu, Andrew Caratenuto, Marilyn L. Minus and Yi Zheng (1)*

Configured with a rapid evaporation rate and a high photothermal conversion efficiency, solar-driven interfacial evaporation displays considerable promise for seawater desalination. Inspired by the versatility and deployability of origami-based structures, we demonstrate a portable waterbomb origami pattern-based tower-like structure, named an "origami tower", as a convertible photothermal evaporator floating on water for efficient solar-driven interfacial desalination. The origami tower has predictable deformability, featuring reversible radial expansion and contraction radially accompanied by small changes in the axial direction. The reversible adjustability of the origami tower offers convenience for transportation and storage, while the quick expansion into its tower shape provides rapid deployment capabilities. Benefiting from an enlarged evaporation surface, excellent light trapping ability, and heat localization, the origami-tower photothermal evaporator yields an evaporation rate of 2.67 kg m⁻² h⁻¹ under one sun illumination. This reversible 3D origami-based photothermal evaporator opens a new avenue for building a portable and efficient solar thermal desalination system.

1 Introduction

Water is the source of all life and the most indispensable liquid in our ecosystem. Adults require an average daily intake of 2.0-3.1 L of clean, safe water for drinking. At present, the desalination of unconventional water sources, such as seawater, brackish water, and municipal wastewater effluent, is a primary method for alleviating the stress on the water supply. There has been rapid growth in large-scale installations of seawater desalination facilities as a means to augment water supplies in water-stressed regions.2-4 Multistage flash distillation and reverse osmosis are two dominant technologies for thermal distillation facilities and membrane-based desalination facilities, respectively, accounting for the majority of the desalination market.5-10 However, the energy-intensive consumption of thermal/electric power and the extensive infrastructure restrict wide spread adoption in sparsely populated rural regions and developing regions to deliver safe and sustainable drinking water. Solar-driven steam generation, where abundant solar energy is harvested as a sustainable source of thermal energy used to purify water directly from seawater, is emerging as a scalable, environmentally benign, and sustainable approach to jointly mitigate the worldwide water crisis. This method can be implemented on vast seawater desalination plants in coastal

Department of Mechanical and Industrial Engineering, Northeastern University, Boston, MA 02115, USA. E-mail: y.zheng@northeastern.edu

† Electronic supplementary information (ESI) available. See https://doi.org/10.1039/d2ta04365c

areas and can also be introduced in small-scale individual applications within remote areas. The development of solar-driven interfacial steam generation has blossomed particularly due to its highly efficient evaporation performance. To date, tremendous research efforts have been made focusing on the development of advanced photothermal materials to enhance photothermal conversion efficiency and the rational design of photothermal evaporator configurations to improve thermal management and water transport. The development of solar-driven areas are supported by the development of advanced photothermal materials to enhance photothermal evaporator configurations to improve thermal

More recently, a flood of three-dimensional (3D) photothermal evaporators has sprung up, making great strides in evaporation rate performance, and far exceeding the theoretical limit of solar-driven steam generation of 1.46 kg m⁻² h⁻¹ of conventional two-dimensional (2D) photothermal evaporation surfaces.23-28 A significant breakthrough is contributed by enlarged evaporation surfaces,29,30 additional energy harvesting from the surrounding air,31-33 utilization of convective airflow,34 and the recycling of latent heat released from water vapor condensation.14 The common geometric configurations of 3D photothermal evaporators, which are either artificially shaped or retain the original figures of the carbonized biomass materials, have been demonstrated in the form of a cylindrical cup,35,36 coil,37 cone,38 umbrella,39 cylinder,40,41 flower,42 block,43 sphere,44,45 etc., which have resulted in a significant improvement in the evaporation performance. 46,47 However, 3D spatial modeling of evaporators tends to occupy more storage space, inflicting additional costs on long-distance transportation and long-term storage. Another possible factor which hinders wide implementation of 3D photothermal evaporators is the

complexity of multi-component assembled structures, which often impairs the long-term stability of the evaporator. As such, the improvement in portability and flexibility will benefit 3D photothermal evaporators for practical applications.

Origami, the art of paper folding, demonstrates the art of spatial geometrical transformation, providing practical approaches to predictably construct a 3D configuration from a pre-designed crease pattern. The crease pattern, known as mountain and valley folding lines, is derived from a 2D planar sheet of paper through a series of folding operations. 48 This structure also enables the origami pattern to be flexible in size and scale, increasing up to the architectural level or decreasing down to the nanometric level. 49-51 The structural integrity of a built origami form is closely related to its geometric characteristics. As such, it is of great interest to dynamically tune the structural parameters of an origami-design through geometrical transformation to meet multiple objectives with a single component. Notably, the property of deployability for the origami, transforming from a 2D initial configuration to a final 3D state, makes the origami-based design desirable for space structures52 and endows origami-based objects with large flexibility in potential deformation modes. Moreover, folded compact systems can be efficiently stored inside the limited dimensions of transportation or storage units and then

deployed in their final desired shape at the destination. Various origami-based designs have been widely applied to reconfigurable structures implemented in numerous fields, such as architecture, ⁵³ robotics, ⁵⁴ aerospace mechanisms, ⁵⁵ antennas, ⁵⁶ *etc.* Among the vast pool of origami patterns, the traditional waterbomb origami pattern, produced from a pattern diagram consisting of a series of vertices where six creases meet, is one of the most widely exploited origami patterns. In addition, the corresponding waterbomb tube, also known as the magic ball, which is made by tessellation of the waterbomb bases has been adopted in the worm robot, robot wheel, and soft gripper. ⁵⁷⁻⁶⁰

In this work, inspired by the flexibility and deployability of origami-based structures, we demonstrate a portable water-bomb origami-based structure as a convertible photothermal evaporator, which floats on water to achieve highly efficient solar-driven interfacial desalination, as shown in Fig. 1. The origami tower is fabricated by folding a sheet of polypyrrole (PPy)-compounded cellulose paper. Its geometric structure, taking advantage of the predictable deformability of the origami-based design, has the capability to reversibly expand/contract radially, accompanied by relatively small deformations in the axial direction. Thereinto, the commercial hydrophilic cellulose paper is utilized as the framework of the origami tower while PPy is chosen as the photothermal material for achieving

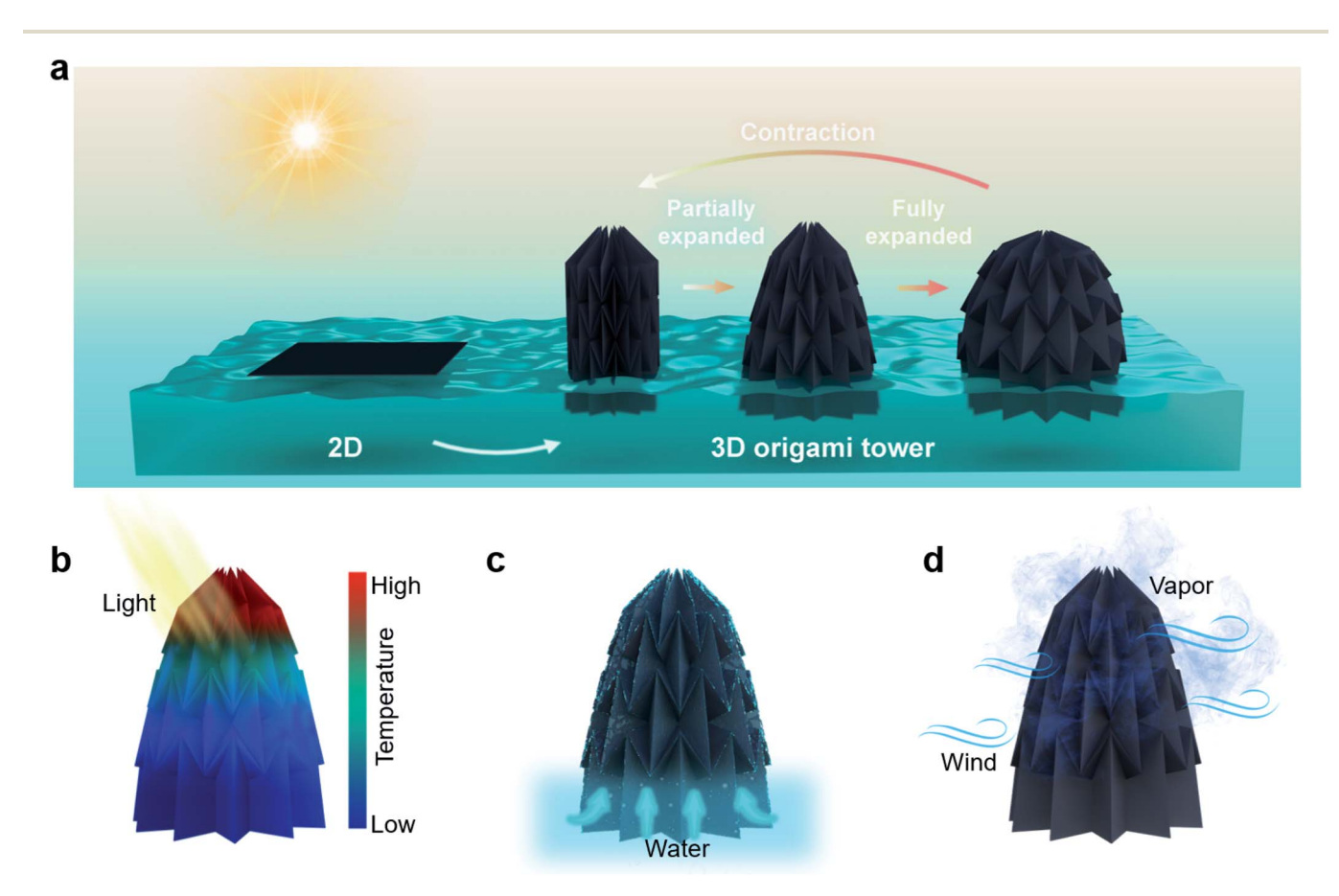


Fig. 1 Schematic illustration of a portable origami tower working as a convertible solar-driven steam generator. (a) Schematic showing the solar-driven evaporators designed in the form of floating 2D membrane and convertible 3D origami towers. (b–d) Schematic demonstration of light absorption, water transportation, and vapor diffusion of the origami tower during the desalination process.

light-thermal conversion. Initially, the origami tower takes on the approximate shape of a cylinder with a pointed top. With gradual expansion of the diameter, the origami-based photothermal evaporator gradually turns into a tower-shaped structure with its base partially submerged in water, the so-called origami tower (Fig. 1a). The origami tower with reversibly changing diameters possesses unique advantages in longdistance transportation and long-term storage. When not in use, the origami tower shrinks to its initial status occupying a smaller space with a regular exterior and can be carried easily. During use, the contracted origami tower will expand into a tower, taking up more space to perform solar-driven water evaporation more efficiently. This also enables the origami tower, as a photothermal evaporator, to have great potential for practical applications for individuals or small communities in remote areas. Though great optimizations have been achieved, the evaporation performances of traditional floating 2D membrane photothermal evaporators have still not hit the ceiling of theoretical evaporation rates. Here, the 3D origami tower obviously possesses a more effective evaporation interface per unit of projected area, comprising both warm and cold evaporation surfaces. Cold evaporation significantly enhances the overall evaporation performance by drawing energy from the surrounding environment even without solar irradiation. In addition to the light-absorbing properties of PPy, the entire outer surface of the origami tower is riddled with cavities benefiting from the deeply concave surface character of each waterbomb pattern, which enables the evaporator to conduct multiple reflections of the sunlight to enhance the solar absorption (Fig. 1b). Moreover, the hydrophilicity of PPy and porous cellulose paper guarantee a continuous water supply from the bulk water. In addition, the conductive heat loss to the underlying bulk water is restricted through the reduced direct contact area with bulk water compared with a 2D membrane, and the encapsulated air and vapor as insulation materials reduce the downward heat dissipation (Fig. 1c). Additionally, vapor diffusion equally requires attention in the evaporation performance, otherwise, the temperature of the evaporation surface will be too high and thermal radiation and convection losses will increase (Fig. 1d).

2 **Experimental section**

2.1 Materials

Pyrrole (reagent grade), ammonium persulfate (APS, ACS reagent grade), and sodium chloride (NaCl, 99.0%) were all purchased from Sigma-Aldrich, USA. All chemicals were directly used as received without further purification. Cellulose paper with a diameter of 320 mm (grade 1, 180 µm thick) was supplied by WhatmanTM, USA. The white polylactic acid filament with a diameter of 1.75 mm was purchased from Dremel.

2.2 Characterization

The reflectance spectra (UV-visible-near-infrared range: 300 nm-2500) are measured using a Jasco V770 spectrophotometer at an incident angle of 6° with an ISN-923 60 mm BaSO₄

based integrating sphere equipped with PMT and PbS detectors. The reflectance spectra are normalized using a PTFE based reflectance standard. The transmittance spectra (mid-infrared region: 2.5 μm-20 μm) are measured using a Jasco FTIR 6600 spectrometer at a normal incident angle with reference to the background spectrum of a hydraulic pressed KBr film (20 Mpa). Infrared images of samples are taken by employing an FLIR A655SC thermal camera at a resolution of 640×480 with a 25° lens. The airflow velocity is detected by using a HoldPeak 866B digital anemometer. An Extech EC400 ExStik salinity meter is utilized to characterize the salinity of the seawater and collected freshwater samples. The tensile test for cellulose paper is conducted on an RSA-G2 Solids Analyzer (TA Instruments) at a compression rate of 3 mm min $^{-1}$ at room temperature (21 °C).

2.3 Preparation of PPy-compounded cellulose paper

The PPy-compounded cellulose paper was prepared following a previously reported procedure.42 The pristine rectangular cellulose paper with dimensions of 22 cm \times 8 cm was soaked in a pyrrole solution comprising 1 ml of pyrrole and 300 ml of deionized (DI) water. After magnetic stirring at 250 rpm for 10 minutes at room temperature (20 °C), 50 ml of APS solution comprising 3.265 g of APS and 50 ml of DI water was gradually dripped into the pyrrole solution. The reaction for generating PPy attached to the fibers lasts 2 hours, and the magnetic stirring was maintained during the reaction. Then, the blackened PPy-compounded cellulose paper was taken out and rinsed with DI water several times until no excess PPy aggregates were attached to the paper. Finally, the composite sheet was dried in an oven at 60 °C. The step by step folding process of the origami tower is shown in ESI Note S1†.

2.4 Solar steam generation experiments

The steam generation experiments are carried out under a solar simulator (Newport, 94081A, class ABB) which supplies a solar flux of 1 kW m^{-2} with an optical filter for the standard AM 1.5 G spectrum. Solar intensity at the position of the origami tower is measured using a TES 132 solar power meter. DI water and NaCl solutions with various concentrations are prepared at the same initial temperature of 20 °C and placed in 3D-printed plastic beakers with different inner diameters of 30 mm, 40 mm, 50 mm, and 60 mm, respectively. During the evaporation process, the origami tower directly floats on the water with the bottom part immersed in water. To accurately monitor the mass of the water, the evaporation device is placed on an electric balance (RADWAG, PS 1000.X2.NTEP) with a resolution of 0.001 g connected to a computer which enables the recording of the realtime mass change. A fan (Honeywell, HT900) provides the airflow with different velocities. The real-time temperature is monitored using an infrared radiation camera (FLIR, A655sc).

3 Results and discussion

Geometry of the waterbomb-patterned origami tower

The waterbomb-patterned origami tower with radial movement is folded from a sheet of rectangular cellulose paper with

dimensions of 22 cm \times 8 cm. The crease pattern of an initial fully deployed sheet is obtained by tessellating the six-crease waterbomb bases. Subjected to longitudinal compression/ stretching, the tessellation of the waterbomb origami tower in a partially-folded state undergoes continuous deformation, which reflects its configurational tunability. When the two vertical sides of the tessellation are joined together with tape, an origami tower in a fully contracted state is constructed (Fig. 2a).

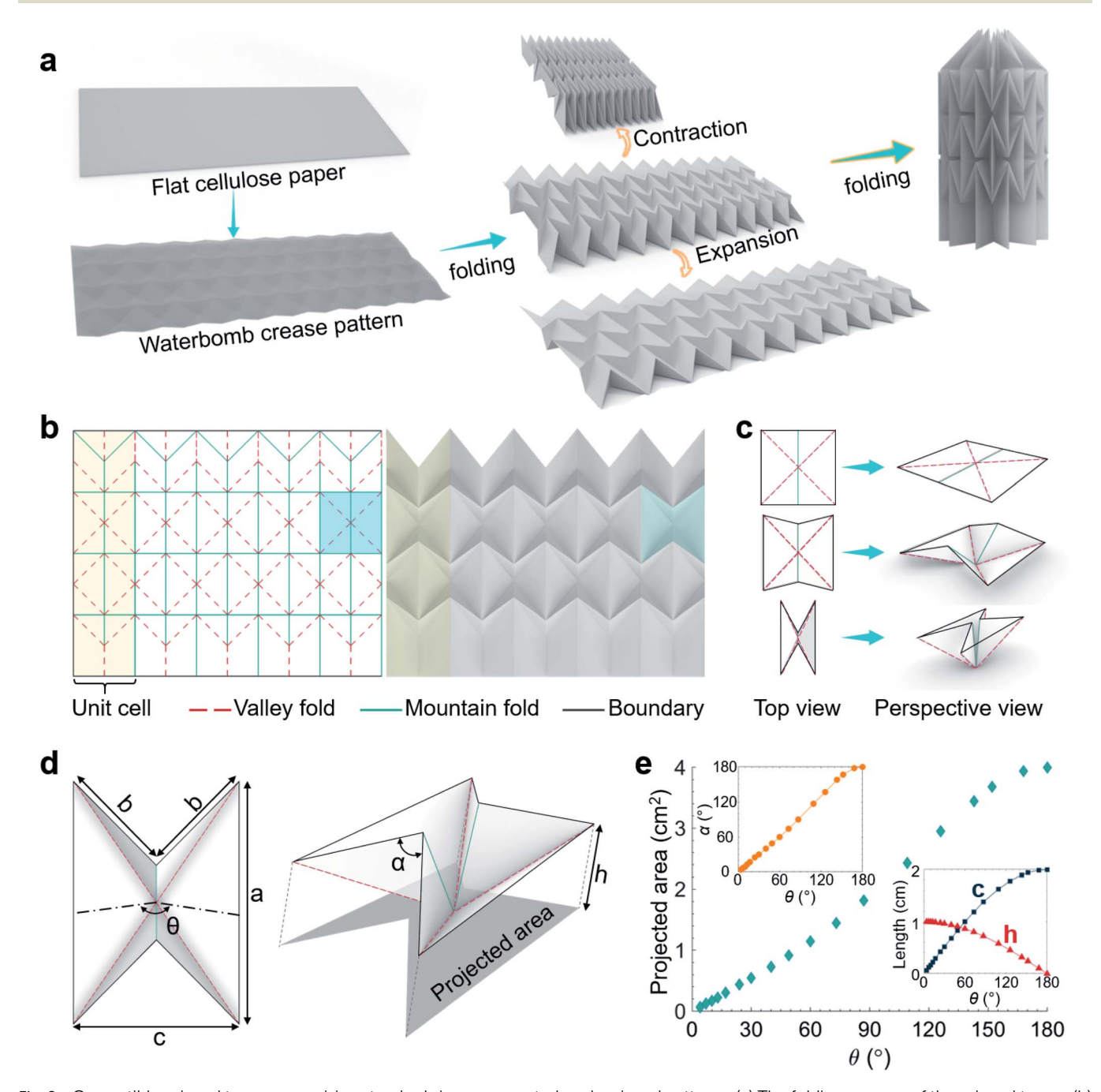


Fig. 2 Convertible origami tower comprising standard six-crease waterbomb origami patterns. (a) The folding process of the origami tower. (b) The 2D crease map (left) and the corresponding 3D configuration (right) of the tessellation for the origami tower. The blue shadowed area represents a standard six-crease based waterbomb pattern. The yellow shadowed area displays a column repeating unit cell that constructs the origami tower. In the crease pattern, the red dashed lines signify the valley folded lines, the green lines signify the mountain folded lines, and the black lines signify the boundaries. (c) Configuration variation of a basic unit of the waterbomb pattern in the top view and perspective view, respectively. (d) The geometric parameters of a waterbomb origami pattern. a and b are the side lengths of the pattern. c is the distance between two vertices. h is the depth of the pattern. θ is the dihedral angle between two mountain slopes. α is the projection angle between two intersecting boundaries. (e) The projected area varies with θ . The projected area refers to the shadow area when the sunlight path is perpendicular to the object. The insets show θ versus α , c, and h, respectively. The dimensions of a waterbomb origami pattern in the initial planar state are 2 cm \times 2 cm.

Part of the waterbomb pattern tessellated crease map of the origami tower is shown in Fig. 2b (left) with 11 repeating columns of unit cells horizontally which is highlighted by the yellow shadow area. In this area, solid lines represent mountain folding and dashed lines represent valley folding. The complete crease map and the folding process for the origami tower in this work are shown in Fig. S1 and S2†. Based on the crease map, also known as the folding line diagram, the 2D flat sheet can be folded into a 3D deployable configuration (Fig. 2b, right). The crease map of a typical waterbomb origami pattern is shown in the blue shadow area in Fig. 2b, and the corresponding 3D folded configuration is shown in Fig. S3†, in different views. In each square unit waterbomb pattern, six creases meet at one central vertex, involving two co-linear mountain creases and four diagonal valley creases, exhibiting symmetry in both horizontal and vertical directions. This pattern is hence identified as a "six-crease" waterbomb (Fig. S4††). Fig. 2c displays the process of the basic unit of a typical waterbomb origami pattern from a plane to a concave structure, rising up from the paper at the mountain creases and sinking back into the paper at the valley creases with the contraction process. Fig. 2d displays detailed geometric parameters of a folded waterbomb origami pattern characterized by the lengths of a and b (a = 2b = 2 cm in this work), a cell width of c, a cell height of h, a dihedral angle of θ , a projection angle of α , and a projected area of A_{proj} , in which, h $= b \times \cos(\theta/2), c = 2b \times \sin(\theta/2), \text{ and } A_{\text{proj}} = a \times c - b \times c \times \sin(\theta/2)$ 2)/tan(α /2). To depict the folding/unfolding deformation process of a waterbomb origami pattern, the dihedral angle (θ) between two mountain slopes in the basic cell is a major consideration, which intuitively reflects the opening degree of the pattern

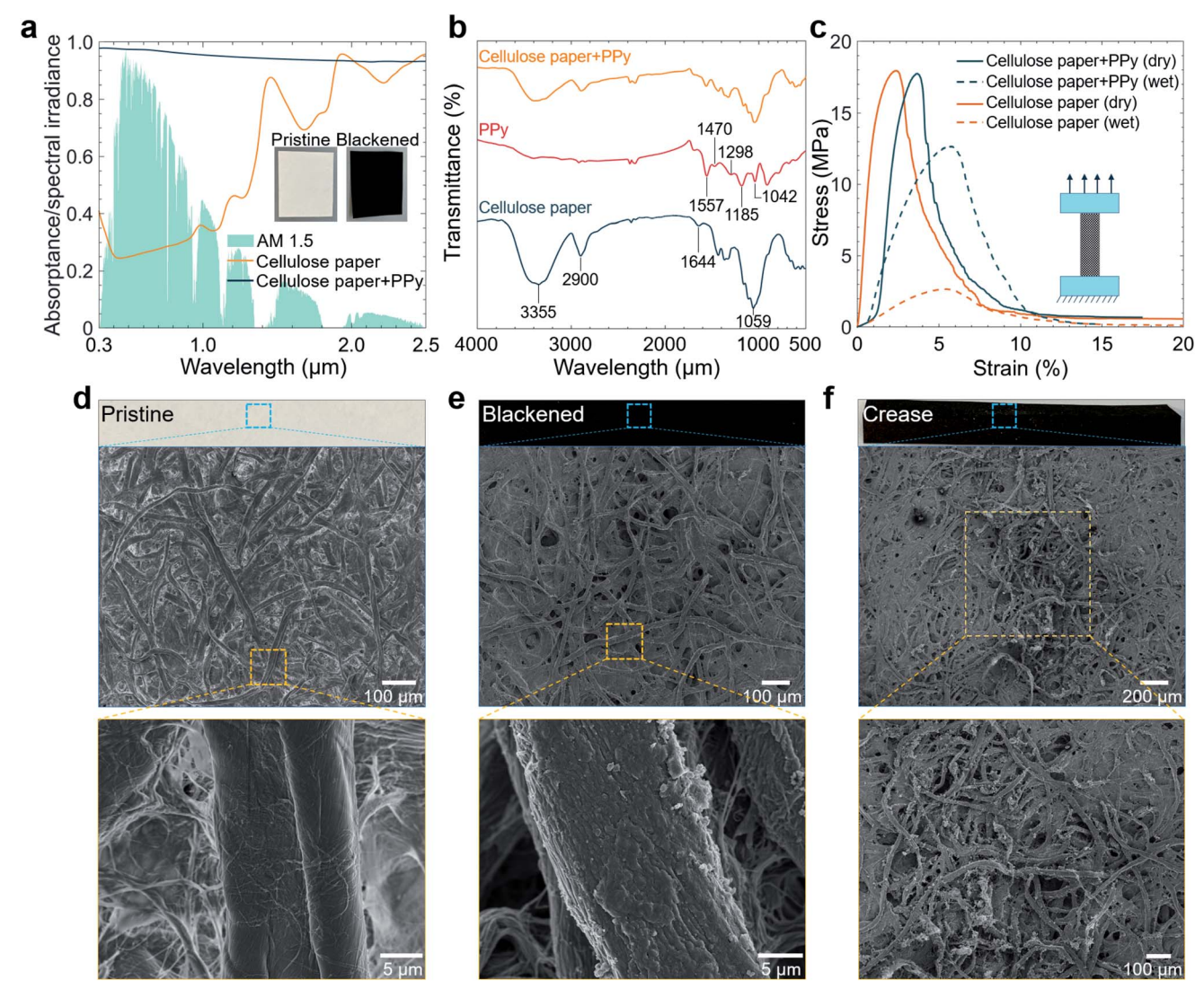


Fig. 3 Characterization studies of the composite membrane. (a) The absorptance spectra of the pristine cellulose paper and the PPy-compounded cellulose paper in a wet state displayed against the AM 1.5 spectral solar irradiance spectrum. (b) FTIR spectra of pristine cellulose paper, PPy powder, and PPy-compounded cellulose paper showing the corresponding chemical composition. (c) Tensile stress-strain curves of pristine cellulose paper and PPy-compounded cellulose paper in the dry state and wet state, respectively. (d and e) Photographs and scanning electron microscopy (SEM) images display the surface morphology of unfolded pristine cellulose paper and PPy-compounded cellulose paper at different magnifications. (f) Optical image and SEM images of the crease of PPy-compounded cellulose paper at different magnifications.

(Fig. 2e). Initially, the basic cell is totally unfolded in a planar state with $\theta=180^\circ$, wherein both projected area $(A_{\rm proj})$, cell width (c), and α are at their maximum values, while the cell height (h) is at its minimum value approximating the thickness of the sheet. When the basic cell starts contracting, θ is reduced, and the $A_{\rm proj}$, c, and α decrease accordingly, making the configuration of the basic cell narrower. However, h increases with the decrease of θ because of the creation of a 3D structure, providing the structure with spatial depth. Finally, the totally compressed basic cell has a near zero value for θ , $A_{\rm proj}$, α , and c. In this case, h reaches its maximum value as a result of the ultimate compression of the basic cell.

3.2 Material characterization studies

The capacity to efficiently absorb solar irradiation is critical for achieving a high solar-driven evaporation rate. Ascribed to the grown PPy on the cellulose fibers⁶¹ and the light trapping effect of disordered and porous fiber networks, the PPy-compounded cellulose paper exhibits excellent light absorption across the solar spectrum with minimal energy loss (Fig. 3a). The visual comparison of the pristine cellulose paper and PPy-compounded cellulose paper elucidates the ultrablack color of PPy which is uniformly coated on the cellulose fibers. Fourier transform infrared (FTIR) spectra elucidate the characteristic absorption peaks of PPy (the red curve) owing to the vibrations of the polypyrrole ring (1557 and 1470 cm⁻¹), in-plane vibrations of the = C-H bond (1298 and 1042 cm^{-1}) and stretching vibrations of the C-N bond (1185 cm⁻¹) (Fig. 3b).⁶² The absorption peaks of cellulose paper (the dark blue curve) result from vibrations of OH group stretching (3355 cm⁻¹), C-H stretching (2900 cm⁻¹), O-H bending of the absorbed water (1644 cm⁻¹), -C-O- groups of secondary alcohols and other functional groups in the cellulose chain backbone (1059 cm⁻¹).⁶³ The stretching strength of the cellulose and composite papers is tested to quantitatively demonstrate mechanical robustness for real-life applications and the associated stressstrain curves are shown in Fig. 3c. The stress-strain curve for the PPy-compounded cellulose paper shows a 4% fracture strain with a stress of 17.8 MPa in the dry state. After absorbing water, the PPy-compounded cellulose paper presents the ultimate tensile strength and a fracture strain of 12.7 MPa and 6%, respectively, indicating its mechanical robustness. Scanning electron microscopy (SEM) is employed to characterize the microscopic structures of the pristine cellulose and the PPycompounded papers. The pristine cellulose paper displays disordered cellulose fibers which form a porous structure, boosting their light trapping photothermal effect due to multiple light reflections (Fig. 3d). The abundance of hydroxyl groups in cellulose, in addition to the micropores in cellulose fibers, allows for rapid water transportation to the evaporation surface, which also facilitates the salt rejection process by providing a path for the salt ions to backflow to the bulk water. The relatively smooth cellulose fiber surfaces become rough after being coated with PPy (Fig. 3e). The PPy content in the blackened cellulose paper after the chemical polymerization process is obtained as 10.17 g m^{-2} , demonstrating the mass of the PPy component attached to the unit area of pristine cellulose. Black PPy enables the absorption and conversion of solar energy into thermal energy to heat the water around it for water evaporation. The effect of the PPy content on the solar-driven evaporation performance is also validated in Fig. S5†. The fabrication of the origami tower necessitates repeated folding and pressing, which inevitably causes some creases on the blackened cellulose paper (Fig. 3f). A small layer of fluff forms on the outer surface of the cellulose paper along the creasing line, but the overall structure is not compromised by this formation, maintaining the origami tower evaporators structural integrity.

3.3 Solar-driven steam generation performance

Geometrically, the origami tower has the capability of radially reversible expansion/contraction with relatively small deformations in the axial direction. The gradual expansion and contraction process of the origami tower with a variable-diameter is schematically presented in Fig. 4a, as depicted by four different intermediate states with maximum diameters, D_{max} , of 30 mm, 40 mm, 50 mm, and 60 mm in the side view and top view, respectively. The evaporation device for the evaporation performance evaluation is composed of a cylindrical water container and an origami tower (Fig. 4b). 3D printed water containers with various inner diameters are employed to confine the maximum diameter of the origami tower into these four intermediate states. Part of the origami tower is immersed in water as a water path pumping water through the porous cellulose fiber network all over the tower for evaporation. The mass change of water through the evaporation device is recorded by an electrical scale under a solar simulator, characterizing its solar-driven steam generation performance. The evaporation rate with a unit of $kg m^{-2} h^{-1}$, that is the mass change of water per unit time per unit projected area, indicates the rate at which the evaporation device produces freshwater, the quantity most commonly used to evaluate evaporative performance. The ambient temperature is about 19 °C and relative humidity is around 29%. The experimental setup is schematically depicted in Fig. 4c. Collimated sunlight from the solar simulator shines on the origami tower that is located at the center of the illumination area on the electrical scale. The surface temperature distributions of the origami tower are captured by an infrared thermal camera. For each experimental period of the evaporation rate measurement, the water mass change is recorded for 90 min, including the first 30 min as the preheating process and the following 60 min as the stable evaporation time. The airflow with various velocities generated by an adjustable fan is employed to evaluate the evaporation performance under forced convection flow.

The efficient photothermal conversion of PPy boosts the evaporation rate greatly. This is depicted obviously by comparing the slopes of the water mass change curves for the pristine and blackened origami towers in Fig. 4d and e, respectively. Only the last 60 min water mass change is displayed, and the change is approximately linear, demonstrating that the evaporation is stabilized after the 30 min preheating

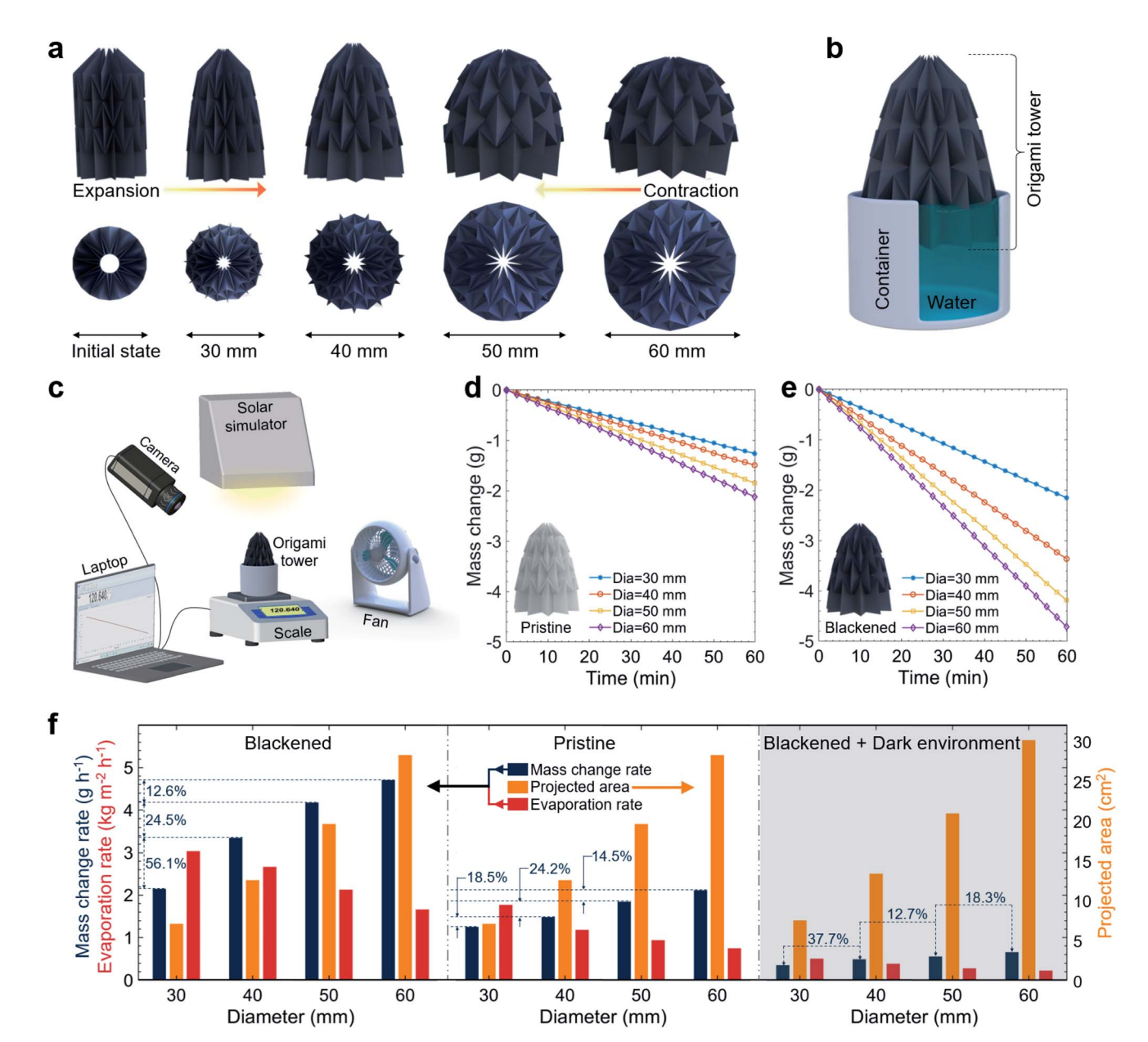


Fig. 4 Convertible origami tower in solar steam generation measurement. (a) Schematic representations of the expansion process (from left to right) and contraction process (from right to left) of the convertible origami tower in the side view (the first row) and top view (the bottom row), respectively. The marked dimensions at the bottom refer to the maximum diameter of the origami tower. (b) Schematic of the evaporation device for solar steam generation in the measurement of the water evaporation rate. The origami tower floats on water with one-eighth of its length immersed in water. A 3D printed cup with different inner diameters functions as the container. (c) Schematic illustration of the experimental setup for the steam generation experiment, involving a solar simulator, an infrared thermal camera, an electrical scale, an electrical fan, a laptop, and the origami tower evaporator. Mass changes of water with the pure cellulose paper-based origami tower (d) and the blackened cellulose paperbased origami tower (e) with different diameters under one sun illumination. The insets show the pristine cellulose paper-based origami tower and blackened cellulose paper-based origami tower with a diameter of 40 mm, respectively. (f) The dependence of the mass change rate (black bar, left y-axis) and evaporation rate (red bar, left y-axis) with the corresponding projected area (orange bar, right y-axis) of the pristine and blackened origami towers with different diameters under solar illumination, and for the blackened ones in the dark environment, respectively. The projected area refers to the area of the origami tower seen from the top view.

time. Similar trends are observed for both the pristine origami tower and blackened origami tower, in that the amount of evaporated water is increased when the D_{max} of the origami towers expands from 30 mm to 60 mm. However, the blackened one exhibits greater slopes of water mass change curves, corresponding to a more efficient photothermal conversion than

that of the pristine one produced by black PPy. Fig. 4f demonstrates the dependence of the water mass change rate with a unit of g h⁻¹, the projected area and the corresponding water evaporation rate of the blackened and pristine origami towers on the diameter of the structures under solar irradiation and in the dark environment, respectively. Overall, the water mass change with the blackened origami tower gradually increases as the D_{max} increases from 30 mm to 60 mm, while the corresponding evaporation rate decreases for larger D_{max} due to the enlarged projected area (Fig. 4f, the histogram on the left). Although the contracted origami tower with a smaller D_{max} shows a higher evaporation rate than that with a larger D_{max} , its water mass change per unit time is lower than that with a larger D_{max} . This mass change rate is greatly increased by 56.1% as the expansion of the origami tower from a $D_{\rm max}$ of 30 mm to a $D_{\rm max}$ of 40 mm occurs. For engineering applications, the smaller mass change of water is not desirable for freshwater collection as the preference for high freshwater yields is primary. According to the percentage growth based on the water mass change rate and balancing of their evaporation rates, the origami tower with a D_{max} of 40 mm is chosen for the following research when compared with other shapes of evaporators. Similar trends are observed for the pristine origami tower (Fig. 4f, the histogram in the middle). To further investigate the relationship between the evaporation rate and water mass change rate, the mass change measurement of the blackened origami tower evaporator is conducted in the dark environment to eliminate the influence of sunlight (Fig. 4f, the histogram on the right and Note S2). The mass changes of the origami tower with a larger D_{max} are higher, while their evaporation rates are lower. For example, the mass change is increased by 37.3% when D_{max} increases from 30 mm to 40 mm. This expansion enlarges the evaporation surface, contributing more vapor generation but reducing the overall efficiency of the structure. Moreover, it also widens the view factor of the valley regions which facilitates vapor diffusion. This dark environment test explains the mass change enhancement during the expansion process from the viewpoint of vapor generation and diffusion. Although the expansion of the origami tower is disadvantageous to the evaporation rate, the contraction/expansion of the origami tower offers more flexibility for transportation and storage. Thus, the transformative structure provides more flexibility to achieve the optimal balance among the freshwater yields, evaporation rate, and space occupation for a variety of use cases.

Due to the 3D geometric structure of the origami tower, the solar illumination conditions over different parts of the tower vary. This is attributed to the varying oblique angles of the structure, which induce various evaporation rates over different regions as a result. The origami tower is geometrically divided into four horizontal portions from top to bottom. These are denoted as the top, middle, bottom, and in-water parts, and are divided by the boundaries of the waterbomb origami patterns. The boundaries of the waterbomb origami patterns located in the middle and bottom parts of the origami tower are highlighted with dashed curves for clarity (Fig. 5a). To investigate the associated mechanism of spatially varying evaporation performance, the overall temperature distributions of the origami tower in the dark and under one sun illumination are characterized using an infrared thermal camera (Fig. 5b). For origami towers with various maximum diameters, the entire outer surface of the tower exhibits an interfacial temperature that is below the ambient temperature in the dark environment

because of the evaporation phenomenon and a solar energy input of zero. Under one sun irradiation, the overall temperature of the outer surface increases above the ambient temperature mainly due to the photothermal conversion effect of PPy coated on the cellulose paper as shown in Fig. S6[†]. In the dark, the occurrence of water evaporation leads to a reduced surface temperature of the origami tower below the ambient temperature as a result of the endothermic process when water evaporation occurs. In this case, the surrounding air at a temperature of 19.3 °C and the bulk water with an initial temperature of 20 °C are the only two energy contributors that can draw heat for water evaporation without solar energy input. Under solar irradiation, the top and middle parts of the origami tower absorb most of the incident solar energy, especially for the tower structure with a larger diameter, which leads to a higher surface temperature compared with the environment. In the indoor evaporation performance tests, the solar light provided by the solar simulator shines vertically on the evaporation device (Fig. S7†). Under solar irradiation, the top area of the origami tower occupies the most favorable position absorbing most of the incident solar energy and converting it into thermal energy. Simultaneously, since the top part is the farthest from the water source (the bulk water), the water supply is not sufficient relative to the middle part and the bottom part, which indicates that it has the least evaporation heat dissipation. Therefore, for the individual origami tower, the top part always possesses a higher temperature distribution under solar irradiation. The side surface of the origami tower does not absorb much solar energy, displaying a relatively lower temperature, and can harvest extra energy from the environment by convective coupling with radiative heat transfer processes, accelerating the evaporation without solar irradiation. This is mainly because evaporative cooling can decrease the temperature of the side surfaces to lower than that of the environment. For a single waterbomb pattern in both the dark environment and solar irradiance cases, the valley region possesses a higher temperature than that of the mountain fold. At the mountain fold, strong evaporation takes place and the generated vapor is in a position to diffuse rapidly into the surroundings. This water evaporation and vapor diffusion take away heat from the evaporation interface of the mountain fold, while vapor generated from the valley region is dense, acting as a thermal barrier between the valley evaporation surface and the ambient environment. This thermal barrier layer slows down the heat dissipation of the valley region. The light-trapping effect within the valley region is another important aspect in explaining this phenomenon. By realizing multiple reflections toward the valley folds, the 3D concave structure of the valley region captures incident light more efficiently compared with the mountain fold, facilitating evaporation with different sun irradiation angles throughout the day. Even without direct solar irradiation, the blackened origami tower with a D_{max} of 40 mm exhibits an evaporation rate of 1.0 kg m⁻² h⁻¹ with diffusive light only (Fig. S8and S9†).

To gain further insight into the spatial temperature distribution at different parts of the origami tower, the surface temperature curves along the central lines of three adjoining

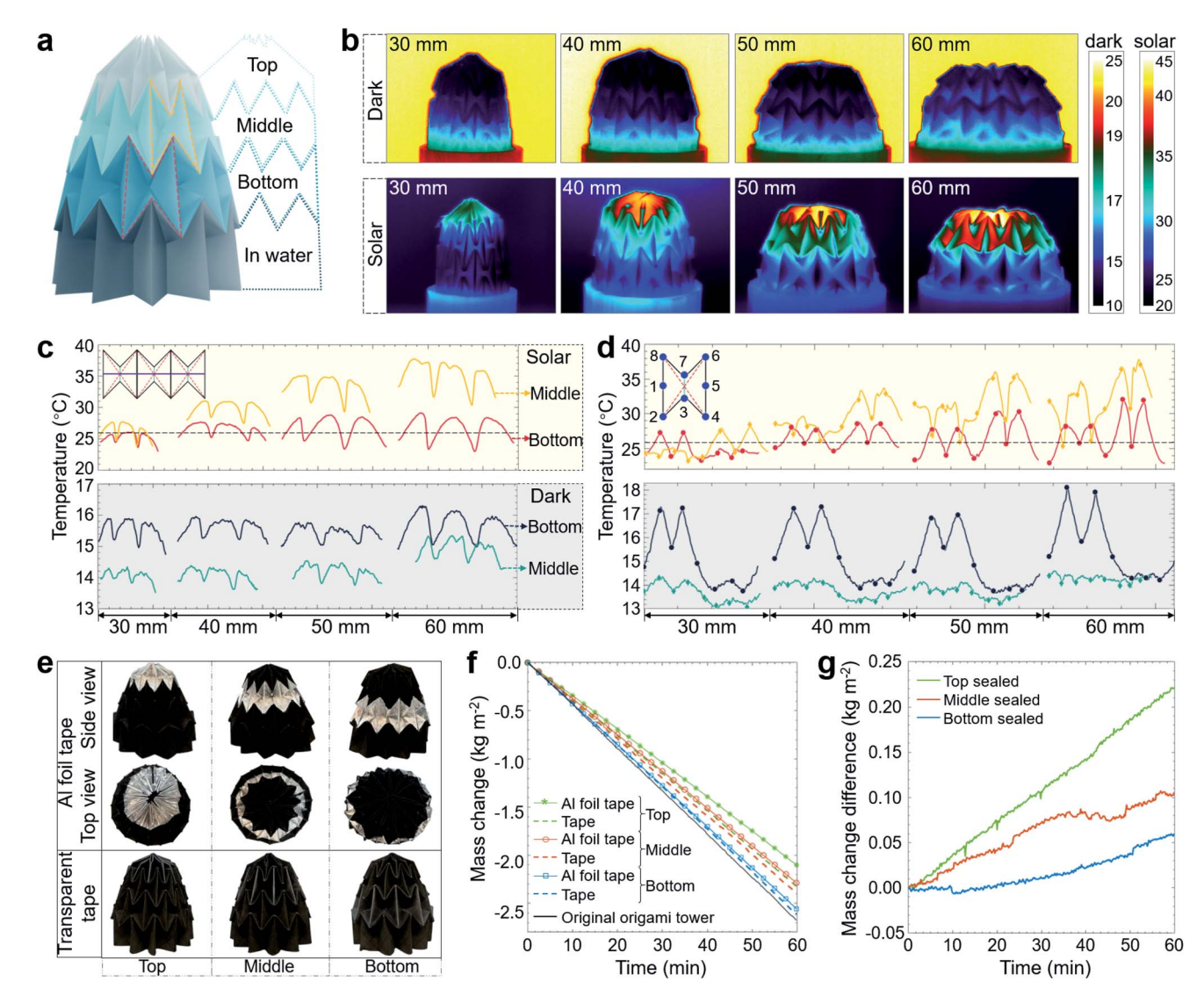


Fig. 5 Solar steam generation performances of the origami tower. (a) Schematic illustrating that the origami tower is divided into top, middle, bottom, and in-water parts. The single waterbomb patterns located in the middle and the bottom parts are highlighted along the boundaries with yellow and red dashed curves, respectively. (b) Infrared thermal images of the origami tower with different diameters in the dark environment (the first row) and under solar irradiation (the second row) after one hour of illumination. (c) The surface temperature distribution along the central lines of the middle and bottom parts (including three adjoining waterbomb patterns) for the origami tower under solar irradiation (the first row) and in the dark environment (the second row), respectively. The purple curve in the inset demonstrates the central line in three adjoining waterbomb patterns. The central curve in one waterbomb pattern starts at the midpoint on one side of the mountain, goes through the valley, and ends at the midpoint on the other side. (d) The surface temperature distribution along the edge of one waterbomb pattern in the middle and bottom parts of the origami tower under solar irradiation (the first row) and in the dark environment (the second row), respectively. The eight solid circles attached on the temperature curve, from left to right, correspond to the nodes, from number 1 to number 8, in the inset. The black dashed lines in (c) and (d) represent an ambient temperature of 26 °C around the origami tower during the desalination process under solar light illumination. In the dark environment, the room temperature is around 19.3 °C. (e) Photographs of the origami towers with different parts (top, middle, and bottom parts) being sealed up using Al foil tape (the first two rows) and transparent tape (the third row), respectively. (f) Mass changes of water with origami towers which are partially sealed up with Al foil tape and transparent tape, respectively. The colors of green, orange, and blue correspond to the parts of the top, middle, and bottom that are sealed individually with tape, respectively. The marked curves show the mass changes of water with the origami tower sealed using Al foil tape, while the dashed curves show the ones sealed using the transparent tape. (g) The time-dependent water mass change differences between the Al foil-sealed origami tower and the transparent tape-sealed origami tower for the top, middle, and bottom parts, respectively.

waterbomb patterns (Fig. 5c and S10†) and the boundary edges of one waterbomb pattern (Fig. 5d and S10†) for the middle and bottom parts are extracted from the infrared images in Fig. 5b. Along the central line, the temperature curves display a repeating connected "saddle shape" with peaks located in the

valley regions. Under solar irradiance, the surface temperature of different parts of the origami tower with various diameters is defined as $T_{D,i}$, where D = 30, 40, 50, and 60 mm and refers to the diameters of the origami towers. The second subscript denotes the middle part (i = m) or the bottom part (i = b). As

shown in Fig. 5c, under solar irradiation, the average temperature difference for central lines between the middle and bottom parts increases when the D_{max} increases, indicating that the corresponding two lines are getting farther and farther apart. For example, $T_{30,m}$ (26 °C) of the middle part is nearly the same as that of the bottom part, $T_{30,b}$ (25 °C), while when the diameter increases, $T_{60,m}$ (34.3 °C) is around 8.6 °C higher than that of the bottom part, $T_{60,b}$ (25.7 °C). This can be attributed to a more efficient thermal localization effect after expansion. Considering the origami tower, the surrounding vapor, and encapsulated air as a system, more vapor and air are enclosed inside the system when the origami tower expands. The vapor and air with thermal conductivities of 26 mW m⁻¹ K⁻¹ and 26.32 mW m⁻¹ K^{−1} at a temperature of 26 °C, respectively, serve as insulators for heat transfer, localizing heat within the top part of the origami tower. This also explains why the top part of the origami towers with different diameters has a higher stagnation temperature under one sun illumination due to the exposure of more area to direct sunlight, while the bottom parts maintain a similar temperature profile (Fig. 5c). In the expansion process with the increasing diameter, the origami tower with the larger diameter exposes more area by opening the waterbomb pattern up to receive more solar light, especially for the top and middle parts (Fig. S11†). When the diameter of the origami tower is larger than 50 mm which is almost completely inflated, the waterbomb patterns in the bottom part are approximately perpendicular to the bulk water surface without direct solar light exposure. In the contracted state, the origami tower has a near-solid compact structure comprising the folded cellulose paper and the absorbed water driven by the capillary force. After expansion, more generated vapor and the air with high temperature are enclosed as an entirety, which can be regarded as a thermal insulator with low thermal conductivity compared with water. Therefore, the top part of the origami tower exhibits higher temperature attributed to the heat localization effect based on the reduced heat loss through convection and downward conduction after expansion. In the dark environment, when the origami tower expands, the average temperature difference for the central lines between the middle and bottom parts shows opposite trends as compared to cases under solar irradiation. Due to the strong cold evaporation, the middle central line always has lower temperatures than the bottom central lines, whose temperatures maintain a similar average value approaching the bulk water temperature, in which, the bulk water can be regarded as a heat source. As the origami tower grows in the radial direction, the structure shrinks in the axial direction i.e., the distance between the heat source and the middle part is shortened. Thus, the heat of the bulk water can easily spread to the middle part making it have a relatively higher temperature when the tower is expanded. To illustrate the spatial temperature distribution of one waterbomb pattern, the temperatures along the boundary edges of a single pattern are extracted and the point labels are shown in the inset of Fig. 5d and S12.† The overall temperature differences between the units in the middle and bottom parts under the solar illumination and in dark environment are similar to the results depicted in Fig. 5c. Under solar irradiation, the peak temperatures of the lower points (points 2 and 4) are lower than those of the upper points (points 6 and 8) for both the middle and bottom parts of nearly all diameters. This trend is reversed for the temperature distribution in the dark environment. These temperature trends result from the spatial location of the heat source. In the case of solar irradiation, the heat source is located at the top of the structure, while in the dark environment case, the bulk water is the relatively high heat source.

With varying temperatures of the top, middle, and bottom parts, their contributions to the overall evaporation rate differ. Aluminum (Al) foil tape and normal clear tape were utilized to seal these sections individually to study their respective evaporative performance (Fig. 5e). The Al foil tape blocks most of the solar irradiation while 90% of solar irradiance can pass through the transparent tape and shine on the origami tower surface (Fig. S13and S14†). Both tapes are vapor-impermeable, preventing vapor diffusion while maintaining water transport. The contribution of distinct components to the evaporation from the sides of photothermal conversion and vapor diffusion can be represented when Al foil tape is used for sealing. The contribution of distinct parts from the viewpoint of vapor diffusion is explored as the transparent tape is used for sealing. The mass change of the top, middle, and bottom parts sealed using Al foil tape and transparent tape is recorded (Fig. 5f). When the top part is sealed using Al foil tape, the reduction of water mass change compared with the unsealed origami tower evaporator is 0.57 kg m⁻², which is much higher than that of the middle (0.38 kg m⁻²) and bottom (0.12 kg m⁻²) parts. This indicates that the top part contributes most of the evaporation for the entire origami tower, which is consistent with the temperature distribution in Fig. 5b. Fig. 5g depicts the timedependent water mass change difference between the Al foilsealed origami tower and the transparent tape-sealed one for different parts. Since both the Al foil tape and transparent tape are vapor-impermeable, this difference exhibits the contribution of these different parts when only considering the photothermal conversion effect. When compared to the middle and bottom parts, the top sealed one provides the largest portion of the evaporation. This indicates potential future improvements for the origami tower evaporator, such as the use of superhydrophilic materials for ample water supply to the top portion.

3.4 Solar desalination of the origami tower and enhanced evaporation under convective flow

The characteristic deep folds within each waterbomb pattern expand the entire outer surface of the origami tower evaporator compared with the 2D planar paper. Derived from the 2D planar paper, the skeleton of the origami tower is an approximate 3D cone with a base radius of $D_{\rm max}$. To validate the advantage of the configuration of the outer surface for the origami tower, evaporation rates of a 2D planar paper, 3D waterbomb-patterned paper, 3D smooth cone with a base diameter of 40 mm and 3D origami tower with a $D_{\rm max}$ of 40 mm are evaluated under one sun illumination (Fig. 6a and S15†). The evaporation rate of the 2D planar paper evaporator is 1.28 kg m⁻² h⁻¹, compared to 0.7 kg m⁻² h⁻¹ for pure water, which is attributed to the additional

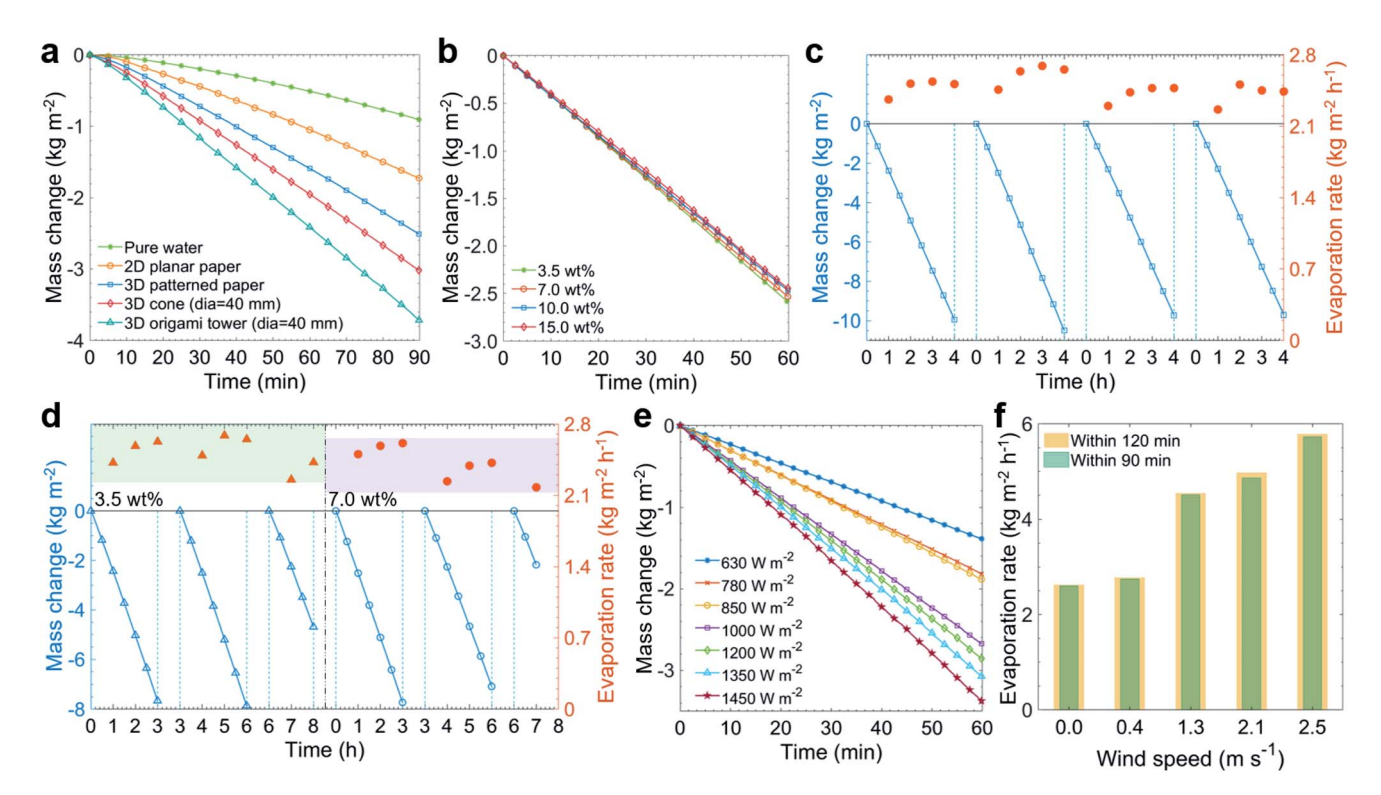


Fig. 6 Solar desalination performance of the origami tower and enhanced evaporation rate under convective flow. (a) Mass changes of water with different shapes of evaporators under one sun irradiation. (b) Mass changes of saline solution with different salinities applying an origami tower with a diameter of 40 mm. (c) The mass changes and the corresponding evaporation rates of water for an origami tower with a diameter of 40 mm using the 3.5 wt% NaCl solution in the repeating long-term desalination tests. (d) The mass changes and the corresponding evaporation rates of water for an origami tower with a diameter of 40 mm using the 3.5 wt% and 7.0 wt% NaCl solutions in the continuous long-term desalination tests. (e) The mass changes of 3.5 wt% NaCl solution for an origami tower with a diameter of 40 mm at different solar intensities. (f) The average overall water evaporation rates with an origami tower (40 mm diameter) applying various airflow speeds.

photothermal conversion and the enhanced evaporation area caused by the porous structure of disordered cellulose fibers in planar paper. Because of the reduced projected area and the localized thermal energy resulting from the air gap between the paper and the water surface, the evaporation rate of the 3D waterbomb-patterned paper reaches 1.79 kg m⁻² h⁻¹. Despite having similar water transportation situations, projected area, and thermal localized effects, the 3D smooth cone has a lower evaporation rate of 2.09 kg $\mbox{m}^{-2}\mbox{ h}^{-1}$ than the 3D origami tower of 2.67 kg m⁻² h⁻¹. The main difference between the 3D cone and the 3D origami tower comes from the concave structures which greatly expand the evaporation surface area. The capability of working in solutions of different salt concentrations can broaden potential working environments across various geographical regions. The evaporation rates of the origami tower evaporator using various saline water solutions are shown in Fig. 6b. No visible salt accumulation is apparent throughout the experiments, which can be attributed to the sufficient water supply to the heating surface and the porous interconnected structure of the filter paper even when using the 15 wt% saline solution as the bulk water under one sun irradiation. When the salt concentration increases from 3.5 wt% to 15 wt%, the evaporation rate swings around 2.5 kg m⁻² h⁻¹, indicating considerable promise for desalination in high-salinity brine. The water safety after solar-driven desalination via the evaporator is a key point to be considered in the industrial production process. To verify this, freshwater water is collected to evaluate the salinity. The seawater collected from Revere Beach, Boston, US, is used as a raw water source. The salinity of water after desalination is dramatically reduced by approximately over three orders of magnitude and is below the drinking water standards defined by the World Health Organization (1%), indicating the effective purification of the seawater (Fig. S16†).

The long-term stability of the water evaporation performance of the 3D origami tower is essential for practical implementations. Thus, an evaporation experiment is performed comprising four 4 hour tests with 3.5 wt% saline solution under one sun irradiation (Fig. 6c). The evaporation rates stabilize at around 2.56 kg m⁻² h⁻¹, illustrating the long-time working durability of the 3D origami tower evaporator. For each 4 hour period, a linear mass change of water is observed, with these four lines of mass change running parallel to each other, demonstrating the 3D origami tower's stable working capability. To evaluate the long-term desalination performance, continuous desalination tests employing 3.5 wt% and 7.0 wt% saline water are conducted (Fig. 6d). Eight consecutive hours and seven consecutive hours of irradiation are applied to the evaporation device with 3.5 wt% and 7.0 wt% saline water, respectively. Eight consecutive hours of experimentation are

composed of two 3 hour and one 2 hour separate experiments for saline water refilling to prevent salinity changes in the bulk water during long-time desalination. Similarly, seven consecutive hours of experimentation are composed of two 3 hour and one 1 hour separate experiments. To further validate the stability of the origami tower, a long-term outdoor evaporation test was performed on the rooftop of the Snell Engineering Center at Northeastern University, Boston, MA, USA, from June 29 to July 11, 2022. A large glass beaker with a diameter of 10 cm and height of 15 cm covers the entire evaporation device placed on the rooftop under solar light for 13 days in a row. The detailed results of the stability test for the photothermal materials/evaporators are described in Fig. S17†. The solar absorptance spectra of the PPy-compounded cellulose paper before and after the long-term outdoor test remain almost consistent even after prolonged exposure to solar light, elucidating the spectrum stability of the photothermal materials attached to the cellulose fibers. The evaporation ability of the origami tower after the test is confirmed by the indoor experiments under one sun irradiation. The mass changes of water with the origami tower before and after the long-term test are close, indicating that the prolonged outdoor work does not obviously affect its evaporation ability and validating the stability of this evaporation device. Clearly, the origami tower can perform in high salinity solutions for long periods of time stably and efficiently. In addition, the intensity of the sun fluctuates during the day and throughout the year. To evaluate the operating performance of the origami tower with a D_{max} of 40 mm under weak and focused sunlight, the evaporation performance under various solar intensities is explored (Fig. 6e). The evaporation rates of the origami tower under an irradiance of 0.63 suns, 0.78 suns, and 0.85 suns are 1.39, 1.82, and 1.88 kg m⁻² h⁻¹, respectively, demonstrating its efficient working capability under weak sunlight. Furthermore, an evaporation rate of 3.38 kg m⁻² h⁻¹ is demonstrated under 1.45 sun illumination, demonstrating the widespread implementation of concentrated solar desalination.

The evaporation process involves two steps of phase transition and vapor diffusion. In the desalination process, the vapor diffuses out of porous materials into the atmosphere during the vapor diffusion process. Generally, the vapor leaves the evaporation interface driven by the vapor concentration gradient from the interface to the environment. As a result, forcing the convective flow to lower the atmospheric vapor concentration is an effective technique for enhancing the occurrence of evaporation. To evaluate the improved vapor diffusion, the evaporation rate at various airflow speeds was studied. Fig. 6f demonstrates the average evaporation rates for the origami tower ($D_{\text{max}} = 40 \text{ mm}$) under one sun irradiation with different incoming airflow speeds for the first 90 min and first 120 min, respectively. Higher airflow speed results in faster vapor diffusion, which is reflected by the increased evaporation rates. For example, the evaporation rate of the origami tower increases from 2.6 to 5.8 kg m⁻² h⁻¹ when the airflow speed increases from 0 m s⁻¹ to 2.5 m s⁻¹. The enhanced evaporation rate of the origami tower under forced convective airflow offers another

approach for higher water vapor yields in engineering applications.

To further validate the outdoor performance of the origami tower-based desalination system under realistic weather conditions, a controlled experiment for the solar desalination test was conducted on the rooftop of the Snell Engineering Center at Northeastern University, Boston, MA, USA, on July 11, 2022 (Fig. S18†). The solar desalination system is composed of a sealed condensation chamber and four origami towers with a diameter of 40 mm which are placed in the water container individually, while only the water is stored inside the water container as a control group without any photothermal materials. The condensation chamber covers the top of the evaporation device to capture the evaporated vapor. Besides, the chamber is made of a polycarbonate board with a thickness of 0.8 mm and an overall transmittance of 83% in the range of solar wavelengths (Fig. S19†). Both the experimental and the control groups of the solar desalination system are placed on polystyrene foam. The average ambient temperature and solar intensity are 27 °C and 684 W m⁻², respectively, during the experimental period from 9:00 to 16:00. The freshwater collection ability of the origami tower-based evaporation device group during the test was 8.55 kg m^{-2} , while that of the control group was only 1.12 kg m^{-2} . The obvious difference between the experimental and control groups validates the good performance of the origami tower-based evaporation device.

4 Conclusions

In summary, we have demonstrated a convertible origami-tower derived photothermal evaporator with waterbomb origami patterns, featuring an evaporation rate of 2.67 kg m⁻² h⁻¹ under one sun illumination with a diameter of 40 mm. The cellulose paper constructs the framework of the origami tower and PPy endows it with a broadband solar absorption, enhanced by the multiple reflections within the deeply concave structures of each waterbomb pattern. The reversible expansion/contraction offers a unique advantage in transportation and storage, while the quick expansion into an origami tower facilitates the fast deployment. Furthermore, the encapsulated air and vapor act as insulation materials, protecting the absorbed energy from dissipating downward to the bulk water. The cold evaporation at the bottom of the origami tower improves overall evaporation performance by collecting energy from the surrounding environment without relying on solar irradiation. High-salinity water (10 wt%) has little impact on the evaporation rate due to the adequate water transportation and salt drainage through the porous structure of cellulose paper. Long-term durability tests demonstrate stable and efficient evaporation performance using 7.0 wt% saline water, which shows considerable promise for high-salinity evaporation applications. The enhanced evaporation rate under forced convective airflow offers a new possibility for improving freshwater yields. Taking advantage of the expanded evaporation surface, light trapping effect, heat localization, and rapid salt drainage, the origami-tower photothermal evaporator provides a promising prototype for efficient solar desalination.

Author contributions

X. L., Y. T., and Y. Z. conceived the initial concept. X. L., Y. T., and F. C. performed the desalination experiments. Y. M. and A. C. conducted the characterization experiments and analyzed the corresponding data. All authors discussed the results and commented on the manuscript. Y. Z. supervised this project.

Conflicts of interest

There are no conflicts to declare.

Acknowledgements

This project was supported by the National Science Foundation through grant number CBET-1941743.

Notes and references

- 1 E. Jéquier and F. Constant, Eur. J. Clin. Nutr., 2010, **64**, 115–123.
- 2 M. Elimelech and W. A. Phillip, *Science*, 2011, 333, 712–717.
- 3 Y. Yao, P. Zhang, C. Jiang, R. M. DuChanois, X. Zhang and M. Elimelech, *Nat. Sustain.*, 2021, 4, 138–146.
- 4 Y. J. Lim, K. Goh, M. Kurihara and R. Wang, *J. Membr. Sci.*, 2021, **629**, 119292.
- 5 S. Zhao, Z. Liao, A. Fane, J. Li, C. Tang, C. Zheng, J. Lin and L. Kong, *Desalination*, 2021, 499, 114857.
- 6 S. Cordoba, A. Das, J. Leon, J. M. Garcia and D. M. Warsinger, *Desalination*, 2021, **506**, 114959.
- 7 R. H. Hailemariam, Y. C. Woo, M. M. Damtie, B. C. Kim, K.-D. Park and J.-S. Choi, *Adv. Colloid Interface Sci.*, 2020, 276, 102100.
- 8 A. J. Toth, Membranes, 2020, 10, 265.
- E. Jones, M. Qadir, M. T. van Vliet, V. Smakhtin and S.-m. Kang, Sci. Total Environ., 2019, 657, 1343–1356.
- 10 P. Gleick, Issues Sci. Technol., 1998, 14, 80-88.
- 11 M. Sheng, Y. Yang, X. Bin, S. Zhao, C. Pan, F. Nawaz and W. Que, *Nano Energy*, 2021, **89**, 106468.
- 12 Y. Pang, J. Zhang, R. Ma, Z. Qu, E. Lee and T. Luo, *ACS Energy Lett.*, 2020, 5, 437–456.
- 13 Y. Xia, Y. Kang, Z. Wang, S. Yuan, Y. Li, L. Gao, H. Wang and X. Zhang, J. Mater. Chem. A, 2021, 9, 6612–6633.
- 14 Y. Wang, X. Wu, B. Shao, X. Yang, G. Owens and H. Xu, *Sci. Bull.*, 2020, **65**, 1380–1388.
- 15 X. Liu, Y. Tian, F. Chen, R. Ahlgren, Y. Zheng, M. Su, G. Xiao and Y. Zheng, Sol. Energy Mater. Sol. Cells, 2022, 234, 111436.
- 16 C. Xu, L. Zuo, P. Hang, X. Guo, Y. Pan, G. Zhou, T. Chen, B. Niu, X. Xu, Z. Hong, et al., *J. Mater. Chem. A*, 2022, **10**, 9971–9980.
- 17 M. Zhang, F. Xu, W. Liu, Y. Hou, L. Su, X. Zhang, R. Zhang, L. Zhou, X. Yan, M. Wang, et al., *Nano Res.*, 2022, 1–6.
- 18 F. Nawaz, Y. Yang, S. Zhao, M. Sheng, C. Pan and W. Que, *J. Mater. Chem. A*, 2021, **9**, 16233–16254.
- 19 L. Zang, L. Sun, S. Zhang, C. Finnerty, A. Kim, J. Ma and B. Mi, *Chem. Eng. J.*, 2021, **422**, 129998.

- 20 Q. Zhang, X. Xiao, G. Zhao, H. Yang, H. Cheng, L. Qu, W. Xu and X. Wang, J. Mater. Chem. A, 2021, 9, 10945–10952.
- 21 I. Ibrahim, D. H. Seo, A. M. McDonagh, H. K. Shon and L. Tijing, *Desalination*, 2021, **500**, 114853.
- 22 P. He, H. Bai, Z. Fan, L. Hao, N. Liu, B. Chen, R. Niu and J. Gong, *J. Mater. Chem. A*, 2022, **10**, 13378–13392.
- 23 C. Wei, X. Zhang, S. Ma, C. Zhang, Y. Li, D. Chen, H. Jiang, Z. Xu and X. Huang, *Chem. Eng. J.*, 2021, 425, 130118.
- 24 T. Wang, S. Gao, G. Wang, H. Wang, J. Bai, S. Ma and B. Wang, *J. Colloid Interface Sci.*, 2021, **602**, 767–777.
- 25 Z. Xie, J. Zhu and L. Zhang, *ACS Appl. Mater. Interfaces*, 2021, 13, 9027–9035.
- 26 H. Li, W. Zhu, M. Li, Y. Li, R. T. Kwok, J. W. Lam, L. Wang, D. Wang and B. Z. Tang, Adv. Mater., 2021, 33, 2102258.
- 27 M. He, H. Dai, H. Liu, Q. Cai, Y. Liu, L. Wang, X. Qin and J. Yu, *ACS Appl. Mater. Interfaces*, 2021, 13, 40664–40672.
- 28 B. Shao, Y. Wang, X. Wu, Y. Lu, X. Yang, G. Y. Chen, G. Owens and H. Xu, *J. Mater. Chem. A*, 2020, **8**, 11665–11673.
- 29 Y. Wang, X. Wu, P. Wu, J. Zhao, X. Yang, G. Owens and H. Xu, *Sci. Bull.*, 2021, **66**, 2479–2488.
- 30 Z. Xu, X. Ran, D. Wang, M. Zhong and Z. Zhang, *Desalination*, 2022, 525, 115495.
- 31 X. Li, J. Li, J. Lu, N. Xu, C. Chen, X. Min, B. Zhu, H. Li, L. Zhou, S. Zhu, et al., *Joule*, 2018, 2, 1331–1338.
- 32 W. Li, X. Tian, X. Li, J. Liu, C. Li, X. Feng, C. Shu and Z.-Z. Yu, *J. Colloid Interface Sci.*, 2022, **606**, 748–757.
- 33 X. Wu, Z. Wu, Y. Wang, T. Gao, Q. Li and H. Xu, *Adv. Sci.*, 2021, **8**, 2002501.
- 34 S. Zheng, M. Yang, X. Chen, C. E. White, L. Hu and Z. J. Ren, *Environ. Sci. Technol.*, 2022, **56**(2), 1289–1299.
- 35 Y. Shi, R. Li, Y. Jin, S. Zhuo, L. Shi, J. Chang, S. Hong, K.-C. Ng and P. Wang, *Joule*, 2018, 2, 1171–1186.
- 36 C. Zhang, Y. Shi, L. Shi, H. Li, R. Li, S. Hong, S. Zhuo, T. Zhang and P. Wang, *Nat. Commun.*, 2021, **12**, 1–10.
- 37 Y. Wang, X. Wu, T. Gao, Y. Lu, X. Yang, G. Y. Chen, G. Owens and H. Xu, *Nano Energy*, 2021, 79, 105477.
- 38 Y. Bu, Y. Zhou, W. Lei, L. Ren, J. Xiao, H. Yang, W. Xu and J. Li, *J. Mater. Chem. A*, 2022, **10**, 2856–2866.
- 39 H. Peng, D. Wang and S. Fu, ACS Appl. Mater. Interfaces, 2021, 13, 47549–47559.
- 40 Y. Wang, X. Wu, X. Yang, G. Owens and H. Xu, *Nano Energy*, 2020, **78**, 105269.
- 41 C. Zhang, B. Yuan, Y. Liang, L. Yang, L. Bai, H. Yang, D. Wei, W. Wang and H. Chen, *Sol. Energy Mater. Sol. Cells*, 2021, 227, 111127.
- 42 W. Li, Z. Li, K. Bertelsmann and D. E. Fan, *Adv. Mater.*, 2019, 31, 1900720.
- 43 W. Jonhson, X. Xu, D. Zhang, W. T. Chua, Y. H. Tan, X. Liu, C. Guan, X. H. Tan, Y. Li, T. S. Herng, et al., ACS Appl. Mater. Interfaces, 2021, 13, 23220–23229.
- 44 X. Wu, Y. Wang, P. Wu, J. Zhao, Y. Lu, X. Yang and H. Xu, *Adv. Funct. Mater.*, 2021, **31**, 2102618.
- 45 B. Yuan, C. Zhang, Y. Liang, L. Yang, H. Yang, L. Bai, D. Wei, W. Wang, Q. Wang and H. Chen, *Adv. Sustainable Syst.*, 2021, 5, 2000245
- 46 J. Zhou, Y. Gu, P. Liu, P. Wang, L. Miao, J. Liu, A. Wei, X. Mu, J. Li and J. Zhu, *Adv. Funct. Mater.*, 2019, **29**, 1903255.

- 47 X. Min, B. Zhu, B. Li, J. Li and J. Zhu, *Acc. Mater. Res.*, 2021, 2, 198–209.
- 48 R. J. Lang, Origami Design Secrets: Mathematical Methods for an Ancient Art, CRC Press, 2012.
- 49 P. M. Reis, F. L. Jiménez and J. Marthelot, *Proc. Natl. Acad. Sci.*, 2015, **112**, 12234–12235.
- 50 C. C. Chu and C. K. Keong, AIP Conf. Proc., 2017, 020025.
- 51 H. J. In, S. Kumar, Y. Shao-Horn and G. Barbastathis, 5th IEEE Conference on Nanotechnology, 2005., vol. 2005, pp. 374–377.
- 52 M. Meloni, J. Cai, Q. Zhang, D. Sang-Hoon Lee, M. Li, R. Ma, T. E. Parashkevov and J. Feng, *Adv. Sci.*, 2021, **8**, 2000636.
- 53 A. Sorguç, I. Hagiwara and S. A. Selçuk, *METU J. Fac. Archit.*, 2009, 26(2), 235–247.
- 54 S. Li, J. J. Stampfli, H. J. Xu, E. Malkin, E. V. Diaz, D. Rus and R. J. Wood, 2019 *International Conference on Robotics and Automation* (ICRA, 2019, pp. 7401–7408.

- 55 S. Jape, M. Garza, J. Ruff, F. Espinal, D. Sessions, G. Huff, D. C. Lagoudas, E. A. P. Hernandez and D. J. Hartl, *Smart Mater. Struct.*, 2020, 29, 115011.
- 56 M. Moshtaghzadeh, E. Izadpanahi and P. Mardanpour, *Eng. Struct.*, 2022, **251**, 113399.
- 57 J. Tang, M. Tian, C. Wang, X. Wang and H. Mao, *Mech. Mach. Theory*, 2021, **165**, 104431.
- 58 T. Tachi, M. Masubuchi and M. Iwamoto, Proc. the IASS-APCS Seoul, Korea, 21–24 May, 2012.
- 59 Y. Chen, H. Feng, J. Ma, R. Peng and Z. You, *Proc. R. Soc. A*, 2016, 472, 20150846.
- 60 H. Feng, J. Ma, Y. Chen and Z. You, Sci. Rep., 2018, 8, 1-13.
- 61 C. Li, D. Jiang, B. Huo, M. Ding, C. Huang, D. Jia, H. Li, C.-Y. Liu and J. Liu, *Nano Energy*, 2019, **60**, 841–849.
- 62 Y. Fu, Y.-S. Su and A. Manthiram, J. Electrochem. Soc., 2012, 159, A1420.
- 63 B. Abderrahim, E. Abderrahman, A. Mohamed, T. Fatima, T. Abdesselam and O. Krim, *World J. Environ. Eng.*, 2015, 3, 95–110.